Fatigue crack propagation in additively manufactured porous biomaterials

Hedayati, R.; Amin Yavari, S.; Zadpoor, A. A.

DOI
10.1016/j.msec.2017.03.091

Publication date
2017

Document Version
Accepted author manuscript

Published in
Materials Science and Engineering C: Materials for Biological Applications

Citation (APA)
Hedayati, R., Amin Yavari, S., & Zadpoor, A. A. (2017). Fatigue crack propagation in additively manufactured porous biomaterials. *Materials Science and Engineering C: Materials for Biological Applications*, *76*, 457-463. https://doi.org/10.1016/j.msec.2017.03.091

Original article

Fatigue crack propagation in additively manufactured porous biomaterials

R. Hedayati[1,*], S. AminYavari[1,2], A.A. Zadpoor[1]

[1]*Department of Biomechanical Engineering, Faculty of Mechanical, Maritime, and Materials Engineering, Delft University of Technology (TU Delft), Mekelweg 2, 2628 CD, Delft, The Netherlands*

[2]*Department of Orthopedics, University Medical Centre Utrecht, Heidelberglaan 100, 3584 CX, Utrecht, The Netherlands*

---

[*] Corresponding author, email: r.hedayati@tudelft.nl, rezahedayati@gmail.com, Tel: +31-15-2781021.

Abstract

Additively manufactured porous titanium implants, in addition to preserving the excellent biocompatible properties of titanium, have very small stiffness values comparable to those of natural bones. Although usually loaded in compression, biomedical implants can also be under tensional, shear, and bending loads which leads to crack initiation and propagation in their critical points. In this study, the static and fatigue crack propagation in additively manufactured porous biomaterials with porosities between 66% and 84% is investigated using compact-tension (CT) samples. The samples were made using selective laser melting from Ti-6Al-4V and were loaded in tension (in static study) and tension-tension (in fatigue study) loadings. The results showed that displacement accumulation diagram obtained for different CT samples under cyclic loading had several similarities with the corresponding diagrams obtained for cylindrical samples under compression-compression cyclic loadings (in particular, it showed a two-stage behavior). For a load level equaling 50% of the yield load, both the CT specimens studied here and the cylindrical samples we had tested under compression-compression cyclic loading elsewhere exhibited similar fatigue lives of around 10^4 cycles. The test results also showed that for the same load level of $0.5F_y$, the lower density porous structures demonstrate relatively longer lives than the higher-density ones. This is because the high bending stresses in high-density porous structures gives rise to local Mode-I crack opening in the rough external surface of the struts which leads to quicker formation and propagation of the cracks. Under both the static and cyclic loading, all the samples showed crack pathways which were not parallel to but made 45° angles with respect to the notch direction. This is due to the fact that in the rhombic dodecahedron unit cell, the weakest struts are located in 45° direction with respect to the notch direction.

Keywords: Porous biomaterials; Fatigue behavior; Crack propagation; Additive manufacturing; Biomedical scaffolds.

1. INTRODUCTION

Autologous and allogeneic bone grafts from iliac crest are known as the gold standard for treating large bone defects [1]. However, problems such as donor morbidity, low bone stock availability, and post-surgery complexion has limited their use and given rise to use of synthetic materials [2]. Titanium and its alloys are biocompatible and corrosion resistant materials that have been long used as parts of orthopaedic implants. The much higher stiffness of titanium compared to bone, however, unloads the natural bone around the implant and causes bone resorption. Porous titanium implants, while keeping the excellent biocompatible properties of titanium, have much smaller stiffness values that can be as low as those of natural bone [3]. The interconnected hollow space inside the porous materials also allows for easy body fluid transport and therefore subsequent bone growth inside the porous structure [4, 5].

Additive manufacturing techniques such as selective laser melting (SLM) [6], selective laser sintering (SLS) [7], fused deposition modeling (FDM) [5, 8], and selective electron beam melting (SEBM) [9] have several advantages over traditional manufacturing techniques. These advantages include precise control over the unit cell size and shape, providing the possibility of integrating the solid and porous parts inside an implant, and creating patient-specific implant. While the static properties of additively manufactured porous biomaterials have been usually found in the range of natural bone [5, 10-13], their fatigue properties are more difficult to determine due to their high porosities as well as the defects created during manufacturing processes. Since implants are usually loaded several times in daily activities, understanding their fatigue properties is of importance [14]. Since the porous biomaterials are usually loaded in compression, the few recent studies on their fatigue behavior is dedicated to their fatigue mechanical properties under compression-compression loads [14-17]. Although the weight-bearing implants are usually loaded in compression (to carry body weight), depending on their shape, current position, and direction and magnitude of other external loads, the implants can also be loaded in bending, shearing, and tension which leads to mode-I fatigue crack initiation and propagation. Indeed, even when the porous structure as a whole is under compression, (parts of) individual struts might be under tension.

While no study has been carried out on the crack propagation in the additively manufactured porous structures, there are a few studies in which the fracture toughness and crack propagation properties of traditional foams has been studied. The fracture toughness measurements of Olurin et al [18] on compact tension (CT) specimens showed an R-curve behavior. Tests on specimens with sharp notches showed that their fracture behavior is notch insensitive but is very dependent on the development of crack bridging ligaments behind the crack tip. Kabir et al [19] studied the effect of various parameters such as loading rate, specimen size, crack length, foam density, cell orientation (flow and rise-direction), cross-linking, and solid material properties on the fracture behavior of polymeric foams. They found foam density and the mechanical properties of the solid material the most important parameters in determining the fracture behavior of polymeric foams. More recently, Kashef et al investigated the fracture toughness [20] and fatigue crack growth [21] behavior of open-cell titanium foams manufactured by space-holder method for medical applications. They observed that compared to solid titanium, titanium foams with 60% porosity had a significantly higher Paris exponent, which can be explained by crack bridging and crack closure [21]. They also showed that the fatigue crack grows through the weakest path throughout the foam.

In this study, the static and fatigue crack propagation behavior of additively manufactured porous biomaterials with porosities between 66% and 84% is investigated using CT samples. The samples were made using SLM technique and were tested under tension (in static study) and tension-tension (in fatigue study) loadings. The failure mechanisms were investigated using displacement increment data and damage propagation pathways. To better observe the stress distribution in the samples, finite element (FE) models based on beam elements were also developed and solved.

2. METHODOLOGY

2.1. Experimental tests

Four types of samples were manufactured by selective laser melting method (Layerwise NV., Belgium). All specimens had the same general dimensions of 30 mm × 31.25 mm × 6 mm. The other dimensions of the specimens are shown in Figure 1 that are selected according to standard ASTM E647−13a. The specimens had strut cross-section dimensions between 140 and $251\ \mu m$ and pore sizes between 486 and $608\ \mu m$ (Table 1). The above-mentioned strut and pore dimensions led to relative densities between 16.3% and 33.6% (Table 1 and Figure 2). The specimens were processed on top of a solid substrate in inert atmosphere and were made of the biomedical Ti-6Al-4V ELI titanium alloy spherical powders according to ASTM B348. All the specimens were designed using the same type of repeating unit cell, i.e. rhombic dodecahedron. Each specimen type was first tested under static loading (Instron electropuls e10000 with 10 kN load cell) using a displacement rate of 1 mm/min. The load in the end of the elastic region in the load-displacement curve was measured for each specimen type and a value about half of that value was used as the maximum stress in the cyclic loading. The load ratio (the ratio of the maximum to the minimum load in each loading cycle) was set to $R = 0.1$. All the specimens were tested under tension-tension fatigue. The loading-unloading frequency was set to 15 Hz in all tests.

2.2. Numerical modeling

To better observe stress distribution in the struts of the specimens, FE models (Figure 3) were made and simulated using a commercial package (i.e. ANSYS static standard solver). The FE models had general dimensions similar to those of actual specimens. For each specimen type, the strut size was set to the strut size of the corresponding specimen. Due to presence of irregularities in the cross-section area of the struts in the additively manufactured specimens, the struts of the FE model were discretized using the Timoshenko beam elements with different diameters. Timoshenko beam elements in ANSYS uses linear interpolation and takes transverse shear deformation into account. The strut diameter at each location of the FE model were taken from a Gaussian distribution function whose mean value was taken from the mean value of the manufactured struts (Table 1) and its standard deviation was set to the values measured experimentally (Table 1). The solid part of the manufactured specimens was also created in the FE model and discretized using cubic elements. The DOFs of the neighbor nodes located in the interface between the solid and porous regions in the neighborhood of the grips were coupled to each other. The nodes belonging to the volumetric elements around the lower grip were constrained in all the directions. The nodes belonging to the volumetric elements around the top grip were constrained in X and Z directions and were displaced in Y direction. The displacement values of $d = 0.1, 0.2, 0.3, 0.4,$ and $0.5\ mm$ were considered. $d = 0.5\ mm$ was the maximum displacement below which the experimental load-displacement curve was linear for all the test samples. The mechanical properties of bulk Ti-6Al-4V (Table 2) were used for modeling the mechanical behavior of the struts as well as the solid portions of the specimens.

3. RESULTS

3.1. Experimental tests

Under isostatic loading, all the specimens showed an initial linear part in their load-displacement curve (Figure 4). In this regime, no local damage was observed in the struts. After observing some initial damages in the notch tip of the specimens, the load-displacement curve slope decreased very rapidly and the load-displacement curve reached a maximum point (at displacement range around 0.6-0.8 mm, Figure 4). After this maximum point, all the load-displacement curves showed a decreasing trend. The sharp edges in the load-displacement curves (Figure 4) represent the quick propagation of crack tip from a unit cell to the next. Specimens with lower relative densities exhibited higher number of sharp edges in their load-displacement curve (which demonstrates the discrete crack tip propagation in the specimen) (Figure 4). The specimen with the highest density did not show any sharp edges in the decreasing part of the load-displacement curve that suggests a smooth crack propagation trend (Figure 4). Generally, the maximum load in the load-displacement curve increased by increasing the relative density of the porous structure (F_{max}=211, 552.4, 688.45, and 1141.41 kN for μ=16.3%, 22.9%, 29.9%, and 33.6%, respectively, Figure 4). Increasing the relative density of the porous structure also increased the yielding displacement value (d_y=0.64, 0.69, 0.71, and 0.81 mm for μ=16.3%, 22.9%, 29.9%, and 33.6%, respectively, Figure 4). The maximum displacement (rupture displacement) in the specimens did not show any significant trend with respect to relative density (d_r=2.69, 2.24, 1.66, and 4.09 mm for μ=16.3%, 22.9%, 29.9%, and 33.6%, respectively, Figure 4).

Due to some technical problems, fatigue tests on Ti 120-500 specimen type could only be done on two specimens. All the specimens showed 2-stage displacement-cycle curves (Figure 5). In the first stage, displacement increased very slowly (Figure 5). In the second stage, the displacement increased exponentially (the crack propagated very fast) until the final fracture of the specimen (Figure 5). Generally, the fatigue life of all the specimens was close and between 5,000 and 15,000 cycles (Figure 5). The final fatigue fracture in all the specimens occurred in displacements around 1 mm (i.e. when the displacement reached d_a=1.08-1.41, 0.71-0.94, 0.78-0.95 and 0.78-0.95 mm for μ=16.3%, 22.9%, 29.9%, and 33.6%, mm, the displacement-cycle curve became almost asymptotic). Porous structures with higher relative densities showed more consistent displacement-cycle curves within their three tested specimens. For example, the fatigue lives of the three specimens having relative densities of

33.6% almost coincided with each other (7600-7800 cycles), while the fatigue lives of the specimens having relative density of 22.9% were in the range of 8,981-12,400. The measured fatigue lives was usually higher in structures with lower relative densities (7600-7800 cycles for the highest density structures versus 13248-14335 for the lowest density structure, Figure 5) (note that the load level in all the specimens is 50% of their yielding point obtained from static tests). In all specimens (under both static and cyclic loads), the crack pathway was almost straight and made a 45° angle with the notch direction (for example, see the crack pathway in Figure 6). The experimental results by which Figures 4-5 were plotted can be found in sections S.2 and S.3 accompanying the paper.

3.2. FE simulation

The stress contour of the Ti 170-500 FE model under 0.5 mm displacement of the top grip showed that both the minimum (compressive) and maximum (tensile) stress occur in the area around the crack tip (Figure 7). By increasing the displacement value from 0.1 to 0.5, the stress level in the struts increased. For instance, in the Ti 170-500 model, the maximum stress reached 431, 862, 1290, 1340, 1640 MPa at respectively d=0.1, 0.2, 0.3, 0.4, 0.5 mm. The stress distribution in other cases can be found in section S.1 of the supplementary material accompanying the paper. By changing the applied displacement to values smaller than d=0.5 mm, the measured load was decreased linearly.

4. DISCUSSION

The displacement accumulation diagram obtained for different CT samples under cyclic loading (Figure 5) had several similarities with the corresponding diagrams obtained for cylindrical specimens under compression-compression cyclic loadings [14, 15]. For instance, the displacement accumulation diagram showed a two-stage behavior. Multi-stage strain accumulation diagrams have been observed for porous structures manufactured using both traditional [22, 23] and additively manufacturing techniques [14-16]. The other similarity was that, when the load level was 50% of the yield load, both the CT specimens studied here and the cylindrical specimens we tested under compression-compression cyclic loading elsewhere [14] had similar fatigue lives of around 10^4 cycles. The static diagrams of the CT specimens were, however, different from the cylindrical specimens [14]. The porous structures usually show a long plateau stage in their load-displacement curve while loaded under compression [24]. After the plateau regime, the load starts to increase exponentially because cell edges come into contact with each other (known as densification regime [25]). The CT specimens, however, showed bell-shaped load-displacement curves with their maximum point in their middle part.

The displacement-cycle diagrams showed that for the same load level of $0.5\,F_y$, the lower density porous structures demonstrate longer lives than the higher-density ones. This can be attributed to the difference in the contribution of stress types (axial or bending) generated in the struts of structures with different strut radii. In high-density porous structures (that have thick struts), the bending stress takes a much larger contribution than the axial stress in the total stress generated in the struts. On the other hand, in very low-density structures with thin struts, axial stress usually contributes more to the failure process as compared to the bending stress. The fatigue failures in porous structures (as well as other types of materials) are usually caused by Mode-I crack initiation and propagation in the struts. The high bending stresses in the high-density porous structures give rise to high local Mode-I crack opening situation in the rough external surfaces of the struts which leads to quicker formation and propagation of fatigue cracks. This explains why in the same load level of $0.5\,F_y$, the higher-density porous structures usually have smaller fatigue lives. In static loading, however, local plasticity compensates the high stresses generated by bending stresses.

In this study, FE models were created to observe the stress distribution created in the CT specimens under tensional loading. The FE results showed that both the minimum (compressive) and maximum (tensile) stresses in the lattice structure are created in the struts in the vicinity of the crack tip. The next step in numerical modeling would be the simulation of damage propagation in the porous structures. Such numerical simulation would decrease the study costs to a great amount since the cost of additively manufacturing of several specimens and testing them is still relatively high. The step-by-step damage propagation under compressive loading was carried out in our previous study [15]. In a step-by-step fatigue damage propagation simulation, the number of simulation cycles, N_s, can be lower than the number of cycles it takes for the structure to be failed, N. In the other words, each simulation cycle can consist of a number of loading-unloading cycles, Δn_i. The damage accumulated in the struts in each simulation cycle i can be calculated using Miner's rule [26]. The simulation results, however, showed that very large Δn_i can lead to inaccurate results. In that study, it was shown that the obtained numerical results coincide each other for different Δn_i values, only if "in each solution cycle, Δn_i is chosen in such a way that the number of removed elements is lower than 0.05% of the total number of elements" [15]. Despite the attempts to decrease computational time, a complete fatigue damage propagation simulation could take 40 h using a Core i7 CPU and 6 GB RAM. From numerical modeling point of view, the advantage of the CT specimens under tensional load over the cylindrical specimens under the compressive loads is that in the former, the damage area is concentrated around the notch tip. Therefore, in the CT structures, modeling the microstructure of the lattice structure around the notch tip would be sufficient. A multi-scale model with two different zones would be suitable for such purpose: (a) a micro-scale zone around notch tip in which the micro-structure of the porous structure is modeled at the strut level, and (b) a macro-scale zone covering the rest of the specimen in which large brick elements with elastic mechanical properties of the porous structure are used for discretization.

Under both static and cyclic loads, all the specimens showed crack pathways which made 45° angles with the notch direction. The solid materials, however, usually show straight crack pathways that are parallel to the notch direction [27-30]. In porous CT specimen extracted from foam panels made by traditional techniques (which usually have more non-homogenous microstructure compared to additively manufactured porous structures), the crack pathway was not straight and the main crack tip usually changed direction through the weakest path [31]. The numerical simulations carried out in this study showed that the weakest struts are located in 45° direction with respect to the notch direction (Figure 7). Unlike the relatively irregular unit-cells in the porous structures made by traditional foaming methods, the weakest direction in each rhombic dodecahedron unit cell made by additive manufacturing technique is always in 45°. That is why the crack continues to propagate in the same 45° direction until the final fracture. Another interesting point was that the 45° crack pathways were always formed in the upper half of all the specimens. This can be attributed to the non-symmetrical stress distribution in the porous structure under tension. Ideally, it is supposed that the stress distribution is symmetrical with respect to the notch direction (and it is usually so in solid materials). Since in the porous structures, the load is transferred from the top grip to the lower grip through very thin struts of the lattice structure, the upper half of the structure “feels” and therefore is damaged by external load prior to the lower half of the specimen. In other words, the struts located in the upper half of the structure usually have higher deformation and earlier permanent plastic damage. Remember that unlike the bulk materials, the additively manufactured porous structures always show some degrees of plasticity even under small amounts of load (due to the fact that there are always points in the surface of the struts which have very high stress concentration degrees). Since the load is imposed on the top grip, the degree of progressive permanent plastic damage is higher in the top half of the specimen. This fact was also verified by numerical simulations which showed higher load levels in the upper half of the unit cell located in the notch tip compared to the load level in its lower half (compare 1640 MPa to -1340 MPa in Figure 7). By increasing the relative density of a porous structure, since the specimen becomes stronger, the effect of micro-plasticity in the outer surface of the struts becomes less (because the ratio of surface roughness to the strut radius decreases). It is therefore expected that the 45° pathway is less distinguished in it (in fact the porous structure becomes more similar to a solid material which shows a crack pathway parallel to the notch direction). This hypothesis was verified by comparing the crack pathways in the lowest-density and the highest-density porous structures. While in the Ti 170-450 (μ=22.9%) specimen, the crack direction was 45° from almost the notch tip, in the Ti 230-500 (μ=33.6%) specimen, it took the crack pathway to pass a few unit cells before it became completely 45° (see Figure 8).

As the bone new tissues are regenerated inside the pores of the additively manufactured porous structure, they undertake some parts of the load applied to the porous structure. This will decrease the load levels all over the porous structure and as a result in the crack tip. According to our previous study [32], filling an additively manufactured porous structure with a resin with mechanical properties close to those of bone tissue (≈1 GPa) can increase the fatigue endurance limit by 5-8 times depending on the relative density of the porous structure. This increase in endurance limit due to regeneration of bone tissues can be even more extreme in cracks formed from mode-I (opening) loads. That is because bone cells are prone to create micro links in areas with very high curvatures [33] (such as in the crack tip where the damage in the struts create several additional micro-cavities). A future study on this subject would be very helpful on understanding the effect of bone regeneration on the fatigue life of porous biomaterials under mode-I crack propagation conditions.

5. CONCLUSIONS

We studied the static and fatigue crack propagation behavior of additively manufactured porous biomaterials with porosities between 66% and 84% using compact-tension (CT) specimens. The specimens were made using selective laser melting technique and were loaded in tension (in static study) and tension-tension (in fatigue study) loadings. In the cyclic tests, the load level was set to 50% of the yield load obtained from static loading. The results showed that displacement accumulation diagram obtained for different CT specimens under cyclic loading had several similarities with the corresponding diagrams obtained for cylindrical specimens under compression-compression cyclic loadings. For instance, the displacement accumulation diagram showed a two-stage behavior. For load levels equaling 50% of the yield load, both the CT specimens studied here and the cylindrical specimens we tested under compression-compression cyclic loading elsewhere had similar fatigue lives of around 10^4 cycles. The test results showed that for the same load level of $0.5F_y$, the lower density porous structures demonstrate longer lives than the higher-density ones. This can be attributed to the difference in the contribution of various stress types (axial or bending) generated in the struts of structures with different strut radii. While in the low-density structures (with thin struts), the axial (compressive) stresses have the highest contribution in load bearing, in high-density porous structures, the bending stresses have the most influence. The high bending stresses in high-density porous structures gives rise to local Mode-I crack opening in the rough external surface of the struts which leads to quicker formation and propagation of the cracks.

Unlike the crack pathways in CT samples made of metal foams manufactured by traditional techniques which continuously changes direction, in the CT samples manufactured by SLM technique, the crack continues to propagate in the same $45°$ direction until final fracture. This is due to the fact that, as shown by numerical simulations, the weakest struts in the rhombic dodecahedron unit cell are located in $45°$ direction with respect to the notch direction.

ACKNOWLEDGEMENT

We would like to acknowledge the kind support of 3D Systems - Layerwise (http://www.layerwise.com/) for additive manufacturing of the specimens used in the current study.

REFERENCES

1. Oppenheimer, A.J., L. Tong, and S.R. Buchman, *Craniofacial bone grafting: Wolff's law revisited.* Craniomaxillofacial trauma & reconstruction, 2008. **1**(1): p. 49.
2. Pollock, R., I. Alcelik, C. Bhatia, G. Chuter, K. Lingutla, C. Budithi, and M. Krishna, *Donor site morbidity following iliac crest bone harvesting for cervical fusion: a comparison between minimally invasive and open techniques.* European Spine Journal, 2008. **17**(6): p. 845-852.
3. Barbas, A., A.-S. Bonnet, P. Lipinski, R. Pesci, and G. Dubois, *Development and mechanical characterization of porous titanium bone substitutes.* Journal of the mechanical behavior of biomedical materials, 2012. **9**: p. 34-44.
4. Zhang, Z., L. Yuan, P.D. Lee, E. Jones, and J.R. Jones, *Modeling of time dependent localized flow shear stress and its impact on cellular growth within additive manufactured titanium implants.* Journal of Biomedical Materials Research Part B: Applied Biomaterials, 2014. **102**(8): p. 1689-1699.
5. Hedayati, R., M. Sadighi, M. Mohammadi Aghdam, and A.A. Zadpoor, *Mechanical properties of additively manufactured thick honeycombs.* Materials, 2016. **9**(8): p. 613.
6. Warnke, P.H., T. Douglas, P. Wollny, E. Sherry, M. Steiner, S. Galonska, S.T. Becker, I.N. Springer, J. Wiltfang, and S. Sivananthan, *Rapid prototyping: porous titanium alloy scaffolds produced by selective laser melting for bone tissue engineering.* Tissue engineering part c: Methods, 2008. **15**(2): p. 115-124.
7. Traini, T., C. Mangano, R. Sammons, F. Mangano, A. Macchi, and A. Piattelli, *Direct laser metal sintering as a new approach to fabrication of an isoelastic functionally graded material for manufacture of porous titanium dental implants.* Dental materials, 2008. **24**(11): p. 1525-1533.
8. Hedayati, R., M. Sadighi, M. Mohammadi-Aghdam, and A. Zadpoor, *Analytical relationships for the mechanical properties of additively manufactured porous biomaterials based on octahedral unit cells.* Applied Mathematical Modelling, 2017.
9. Heinl, P., L. Müller, C. Körner, R.F. Singer, and F.A. Müller, *Cellular Ti–6Al–4V structures with interconnected macro porosity for bone implants fabricated by selective electron beam melting.* Acta biomaterialia, 2008. **4**(5): p. 1536-1544.
10. Hedayati, R., M. Sadighi, M. Mohammadi-Aghdam, and A.A. Zadpoor, *Mechanical properties of regular porous biomaterials made from truncated cube repeating unit cells: analytical solutions and computational models.* Materials Science and Engineering: C, 2016. **60**: p. 163-183.
11. Hedayati, R., M. Sadighi, M. Mohammadi-Aghdam, and A.A. Zadpoor, *Mechanics of additively manufactured porous biomaterials based on the rhombicuboctahedron unit cell.* Journal of the Mechanical Behavior of Biomedical Materials, 2016. **53**: p. 272–294.
12. Hedayati, R., M. Sadighi, M. Mohammadi-Aghdam, and A. Zadpoor, *Mechanical behavior of additively manufactured porous biomaterials made from truncated cuboctahedron unit cells.* International Journal of Mechanical Sciences, 2016. **106**: p. 19-38.
13. Zadpoor, A.A. and R. Hedayati, *Analytical relationships for prediction of the mechanical properties of additively manufactured porous biomaterials.* Journal of Biomedical Materials Research Part A, 2016.
14. Amin Yavari, S., R. Wauthlé, J. van der Stok, A. Riemslag, M. Janssen, M. Mulier, J.-P. Kruth, J. Schrooten, H. Weinans, and A.A. Zadpoor, *Fatigue behavior of porous biomaterials manufactured using selective laser melting.* Materials Science and Engineering: C, 2013. **33**(8): p. 4849-4858.
15. Hedayati, R., M. Sadighi, M. Mohammadi-Aghdam, and A.A. Zadpoor, *Computational prediction of the fatigue behavior of additively manufactured porous metallic biomaterials* International journal of fatigue, 2016. **84**: p. 67–79.
16. Hrabe, N.W., P. Heinl, B. Flinn, C. Körner, and R.K. Bordia, *Compression‐compression fatigue of selective electron beam melted cellular titanium (Ti‐6Al‐4V).* Journal of Biomedical Materials Research Part B: Applied Biomaterials, 2011. **99**(2): p. 313-320.
17. Lipinski, P., A. Barbas, and A.-S. Bonnet, *Fatigue behavior of thin-walled grade 2 titanium samples processed by selective laser melting. Application to life prediction of porous titanium implants.* Journal of the mechanical behavior of biomedical materials, 2013. **28**: p. 274-290.

18. Olurin, O., N. Fleck, and M. Ashby, *Deformation and fracture of aluminium foams.* Materials Science and Engineering: A, 2000. **291**(1): p. 136-146.
19. Kabir, M.E., M. Saha, and S. Jeelani, *Tensile and fracture behavior of polymer foams.* Materials Science and Engineering: A, 2006. **429**(1): p. 225-235.
20. Kashef, S., A. Asgari, T.B. Hilditch, W. Yan, V.K. Goel, and P.D. Hodgson, *Fracture toughness of titanium foams for medical applications.* Materials Science and Engineering: A, 2010. **527**(29): p. 7689-7693.
21. Kashef, S., A. Asgari, T.B. Hilditch, W. Yan, V.K. Goel, and P.D. Hodgson, *Fatigue crack growth behavior of titanium foams for medical applications.* Materials Science and Engineering: A, 2011. **528**(3): p. 1602-1607.
22. Sugimura, Y., A. Rabiei, A. Evans, A. Harte, and N. Fleck, *Compression fatigue of a cellular Al alloy.* Materials Science and Engineering: A, 1999. **269**(1): p. 38-48.
23. Vendra, L., B. Neville, and A. Rabiei, *Fatigue in aluminum–steel and steel–steel composite foams.* Materials Science and Engineering: A, 2009. **517**(1): p. 146-153.
24. Gibson, L.J. and M.F. Ashby, *Cellular solids: structure and properties*. 1997: Cambridge university press.
25. Li, Q., I. Magkiriadis, and J. Harrigan, *Compressive strain at the onset of densification of cellular solids.* Journal of cellular plastics, 2006. **42**(5): p. 371-392.
26. Miner, M.A., *Cumulative damage in fatigue.* Journal of applied mechanics, 1945. **12**(3): p. 159-164.
27. Oral, E., A.S. Malhi, and O.K. Muratoglu, *Mechanisms of decrease in fatigue crack propagation resistance in irradiated and melted UHMWPE.* Biomaterials, 2006. **27**(6): p. 917-925.
28. Shamili, S., P. Gandhi, S. Vishnuvardhan, and P. Gajalakshmi, *Fatigue Crack Growth Studies on Rail Steel.*
29. Lee, S.Y., E.-W. Huang, W. Woo, C. Yoon, H. Chae, and S.-G. Yoon, *Dynamic Strain Evolution around a Crack Tip under Steady-and Overloaded-Fatigue Conditions.* Metals, 2015. **5**(4): p. 2109-2118.
30. Yi, X., C. Cho, J. Cooper, Y. Wang, M.M. Tentzeris, and R.T. Leon, *Passive wireless antenna sensor for strain and crack sensing—Electromagnetic modeling, simulation, and testing.* Smart Materials and Structures, 2013. **22**(8): p. 085009.
31. Kashef, S., *Biomechanical properties of porous metal scaffolds as implant materials*. 2011, Deakin University.
32. Hedayati, R., M. Sadighi, M.M. Aghdam, S. Janbaz, and A.A. Zadpoor, *How does tissue regeneration influence the mechanical behavior of additively manufactured porous biomaterials?* Journal of the mechanical behavior of biomedical materials, 2017. **65**: p. 831-841.
33. Bidan, C.M., K.P. Kommareddy, M. Rumpler, P. Kollmannsberger, Y.J. Bréchet, P. Fratzl, and J.W. Dunlop, *How linear tension converts to curvature: geometric control of bone tissue growth.* PloS one, 2012. **7**(5): p. e36336.
34. Simonelli, M., Y.Y. Tse, and C. Tuck, *Effect of the build orientation on the Mechanical Properties and Fracture Modes of SLM Ti–6Al–4V.* Materials Science and Engineering: A, 2014. **616**: p. 1-11.

List of tables

Table 1- The porosity, pore sizes, and strut sizes of the four samples tested in this study [14].

	Ti 120-500	**Ti 170-500**	**Ti 170-450**	**Ti 230-500**
Porosity, dry weighing (%)	83.7±0.3	77.1±0.5	70.1±0.3	66.4±0.3
Porosity, Archimedes (%)	83.6±0.3	76.8±0.5	69.7±0.3	65.8±0.3
Porosity, micro-CT (%)	84.22	77.68	71.20	68.45
Pore size, nominal (μm)	500	500	450	500
Pore size- micro-CT (μm)	560±173	608±182	486±162	560±186
Strut size, nominal (μm)	120	170	170	230
Strut size, micro-CT (μm)	140±38	218±62	216±64	251±76

Table 2- The material properties of Ti-6Al-4V used in numerical modelling [34]

	Ti 120-500
Elastic modulus, GPa	113.8
Tangent modulus, GPa	1.25
Yield stress, MPa	1000

Figure captions

Figure 1- Dimensions of the manufactured samples

Figure 2- Samples with different porosities and unit cell sizes tested in this study

Figure 3- The (a) 3D and (b) front views of the FE model used for numerical simulation. The upper and lower struts of the nodes marked by red circles in (b) are not tied together and can therefore be easily separated if the sample is loaded in tension.

Figure 4- Comparison of load-displacement curves under static loading for different samples tested in this study

Figure 5- Comparison of displacement vs. cycle diagrams for different sample types under cyclic loading

Figure 6- Damage propagation in CT specimen Ti 170-450 under fatigue loading under different displacement values (a) 0.5 mm, (b) 0.61 mm, (c) 0.68 mm, and (d) 4.14 mm.

Figure 7- Stress distribution in the FE model under 0.5 mm displacement of the upper grip (Units are in Pa). The stress distribution in each strut is representative of accumulation of axial and bending stresses generated inside it.

Figure 8- Comparison of crack pathways in (a) Ti 230-500 ($\boldsymbol{\mu = 33.6}\%$) and (b) Ti 170-500 ($\boldsymbol{\mu = 22.9}\%$) samples

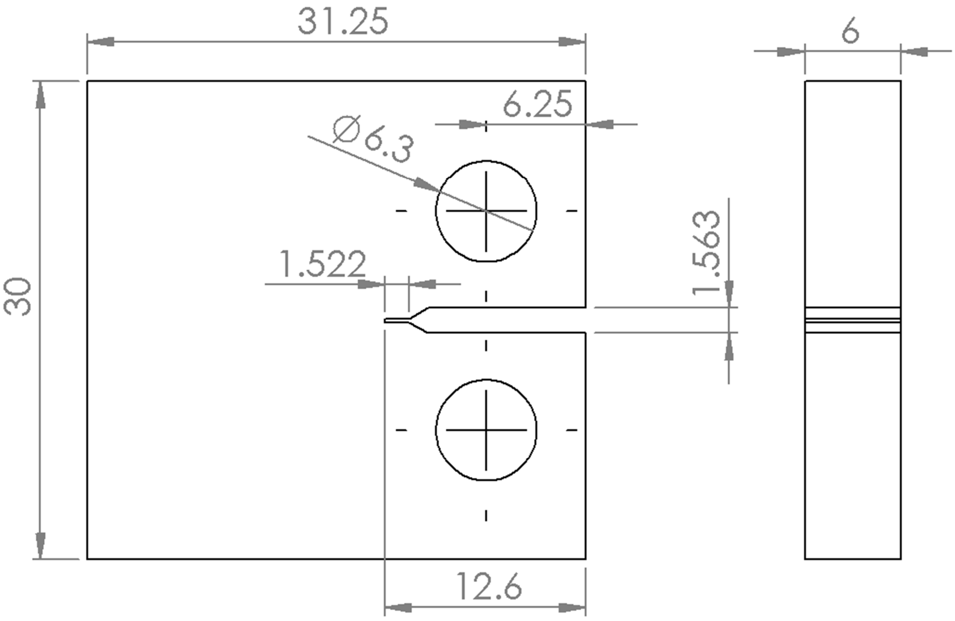

Figure 1- Dimensions of the manufactured samples in mm

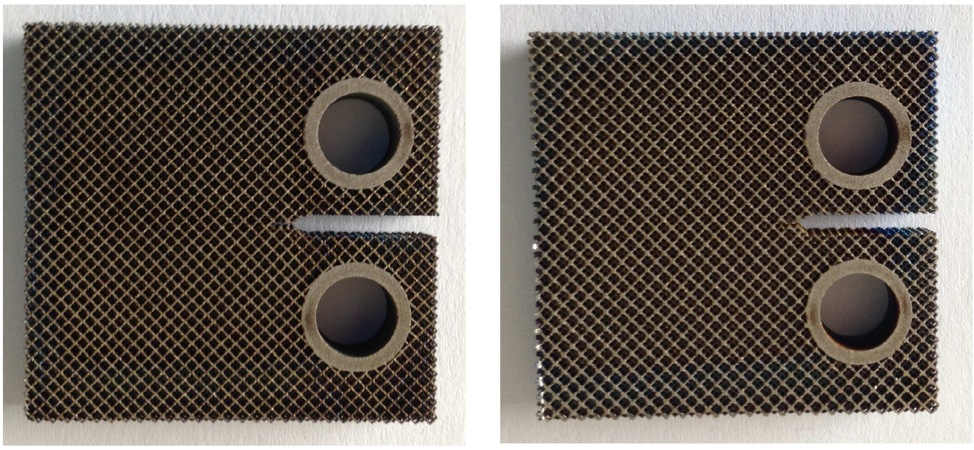

(a) Ti 120-500 (b) Ti 170-500

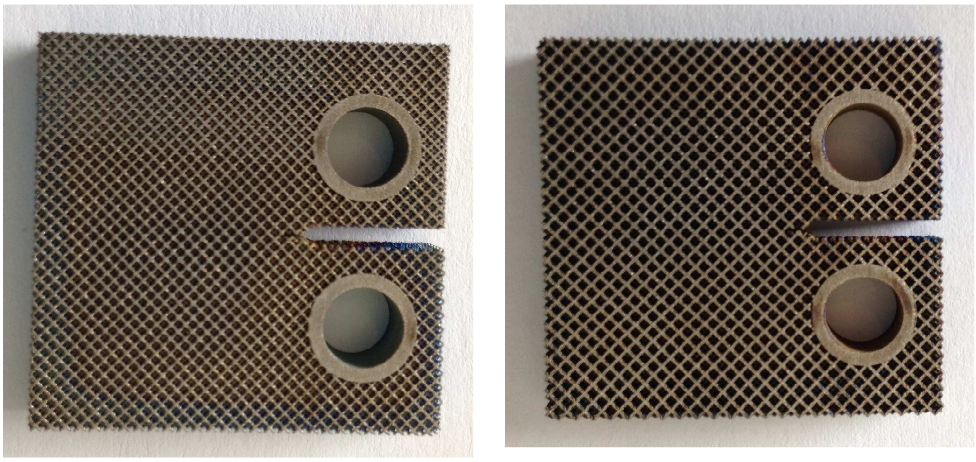

(c) Ti 170-450 (d) Ti 230-500

Figure 2- Samples with different porosities and unit cell sizes tested in this study

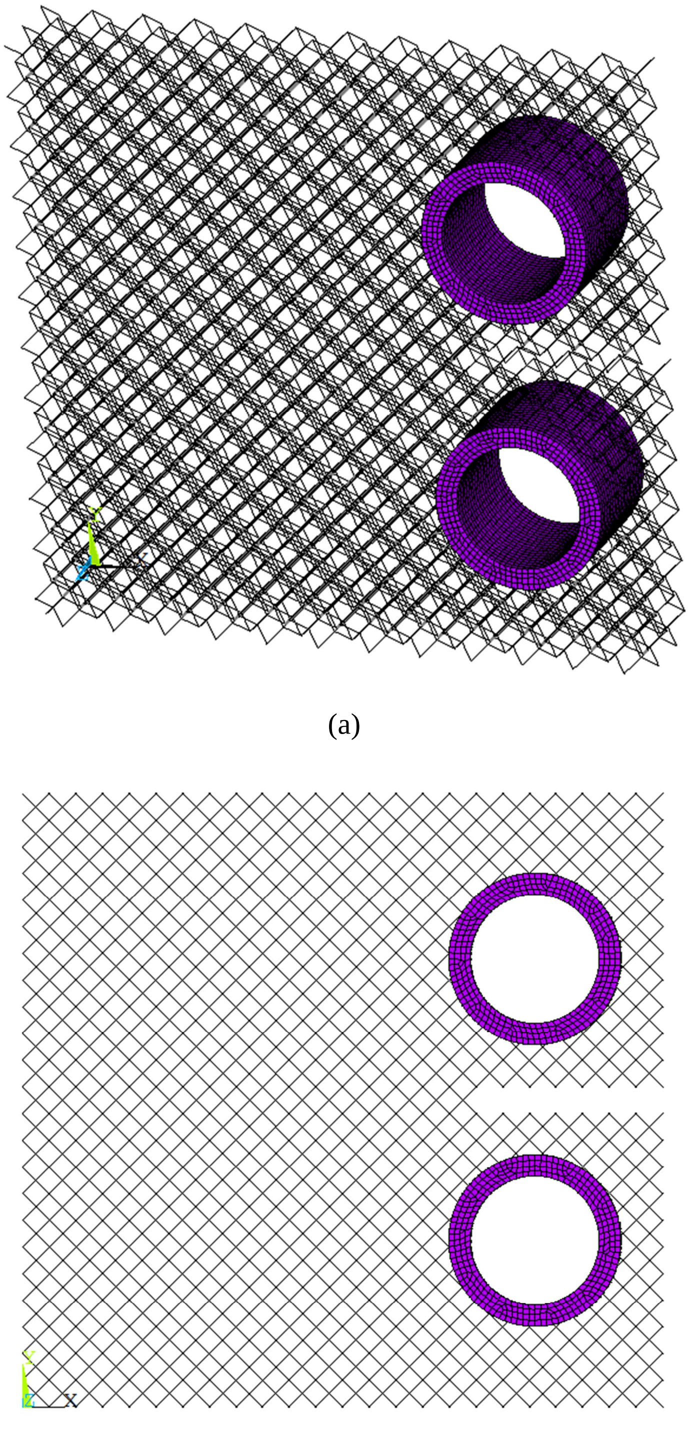

(a)

(b)

Figure 3- The (a) 3D and (b) front views of the FE model used for numerical simulation. The upper and lower struts of the nodes marked by red circles in (b) are not tied together and can therefore be easily separated if the sample is loaded in tension.

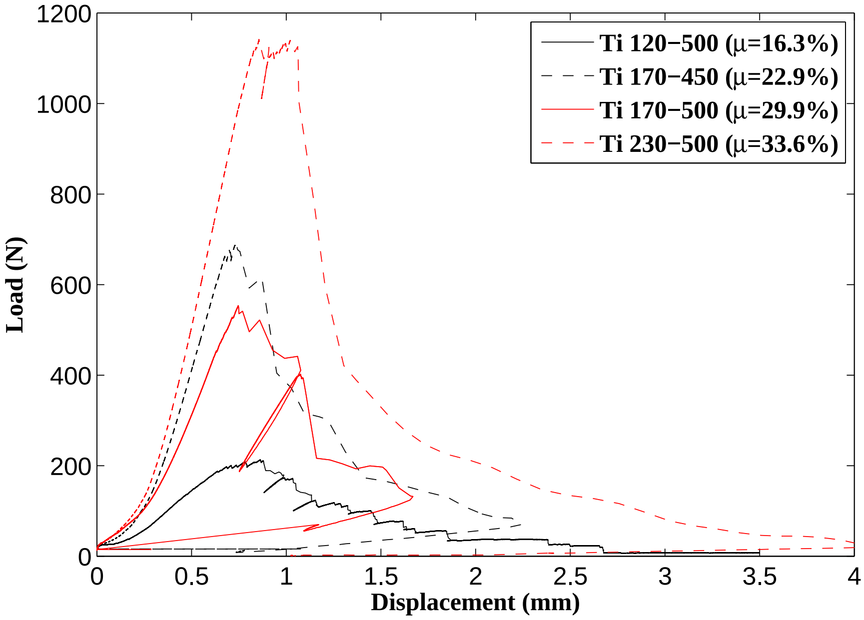

Figure 4- Comparison of load-displacement curves under static loading for different samples tested in this study

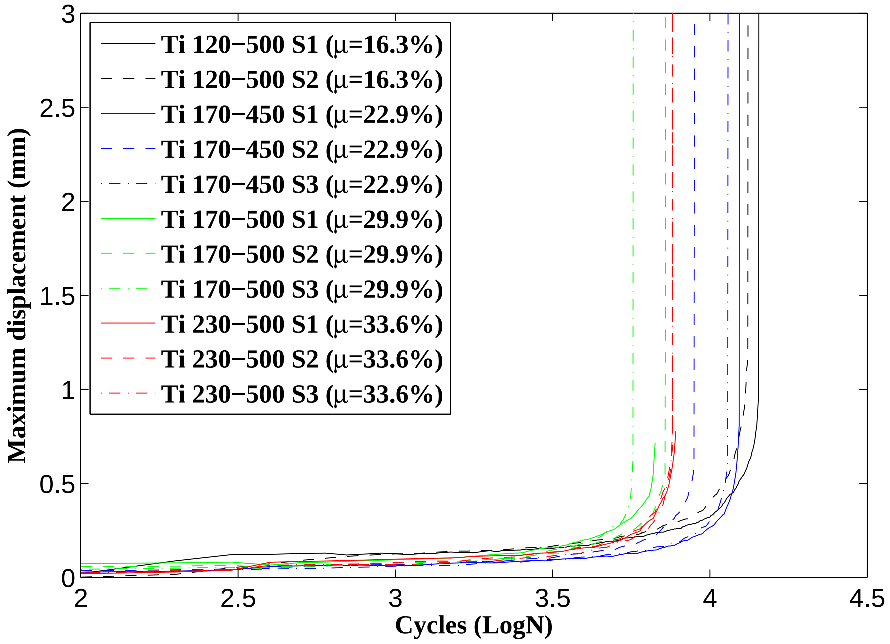

Figure 5- Comparison of displacement vs. cycle diagrams for different sample types under cyclic loading

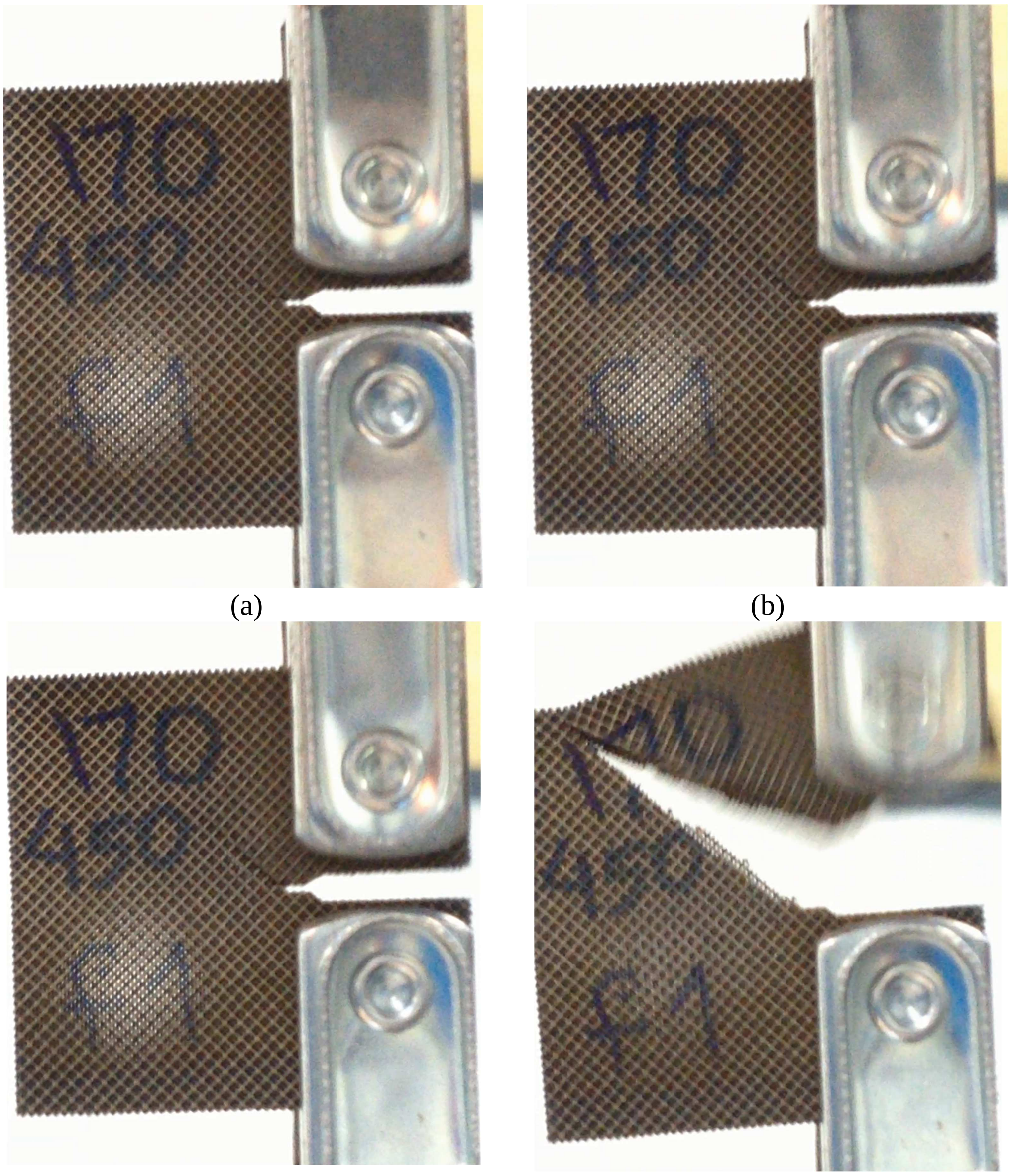

(a) (b)

(c) (d)

Figure 6- Damage propagation in CT specimen Ti 170-450 under fatigue loading under different displacement values (a) 0.5 mm, (b) 0.61 mm, (c) 0.68 mm, and (d) 4.14 mm.

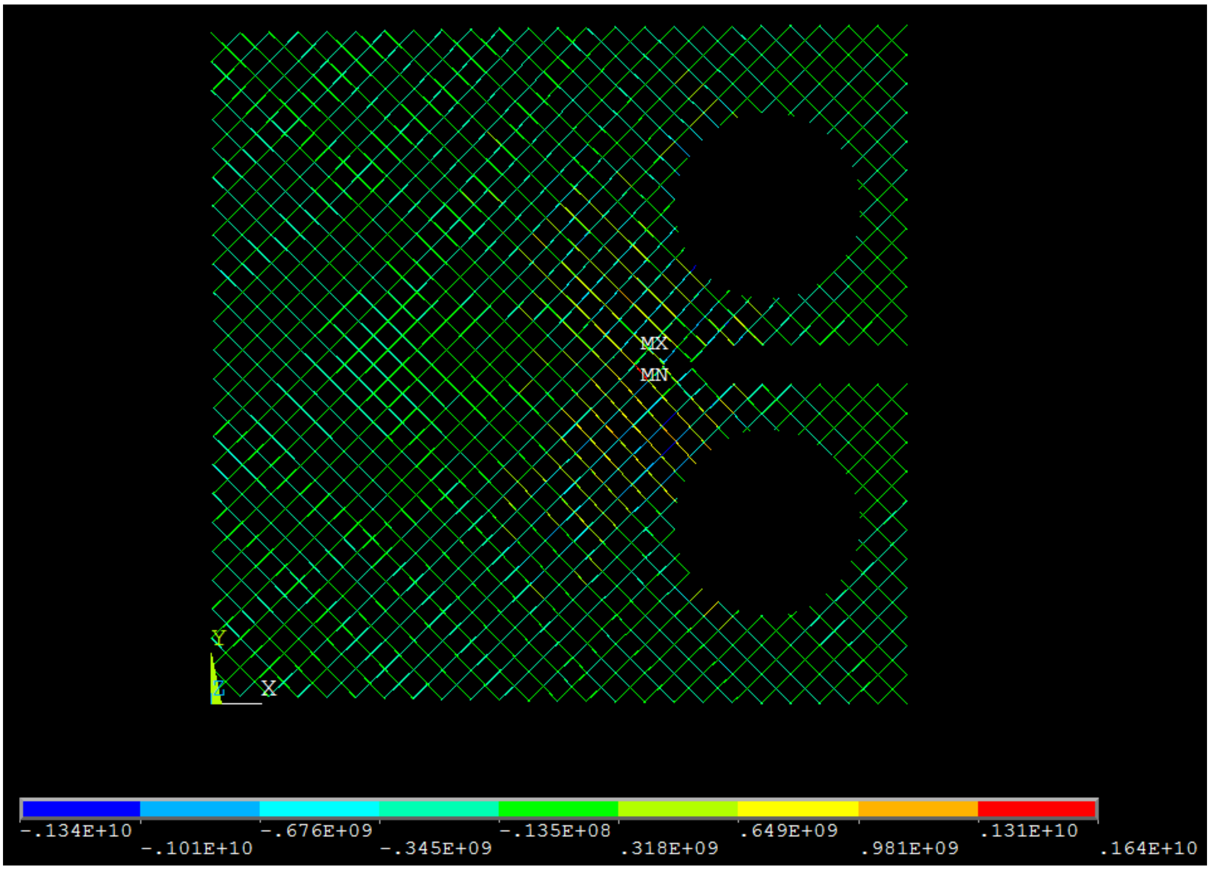

Figure 7- Stress distribution in the FE model under 0.5 mm displacement of the upper grip (Units are in Pa). The stress distribution in each strut is representative of accumulation of axial and bending stresses generated inside it.

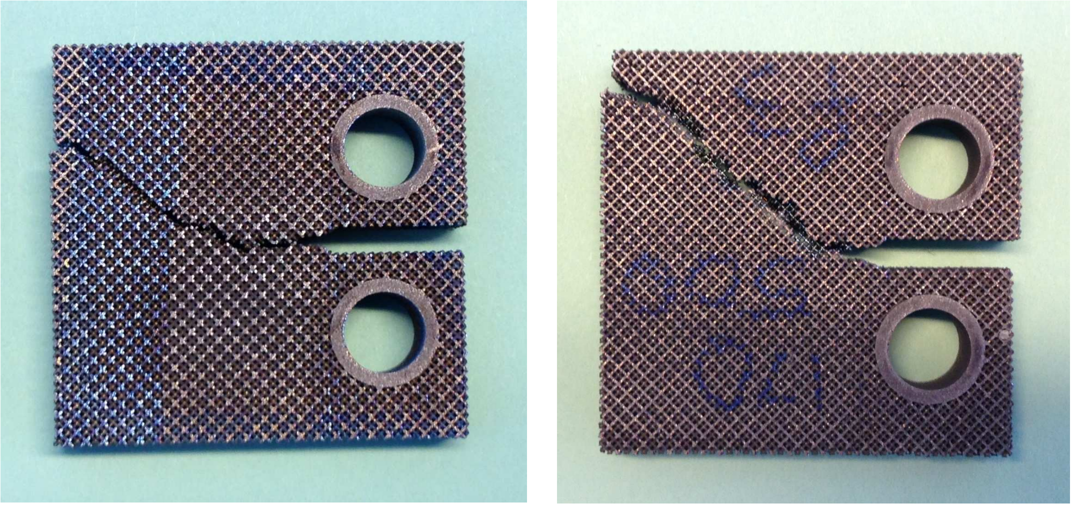

(a) **(b)**

Figure 8- Comparison of crack pathways in (a) Ti 230-500 ($\mu = 33.6\%$) and (b) Ti 170-500 ($\mu = 22.9\%$) samples